Robotica (2026), **44**, pp. 723–738
doi:10.1017/S0263574726103294

CAMBRIDGE UNIVERSITY PRESS

RESEARCH ARTICLE

Multi-objective optimization of a dish parabolic concentrator with a parallel sun-tracking mechanism

Shen Yao, Fanmao Liu, Han Mo, Hanlin Gong, Yunlong Chen and Tao Yang

School of Mechanical Engineering, Hunan University of Science and Technology, Xiangtan, Hunan, China
Corresponding Author: Fanmao Liu; Email: liufanmao@hotmail.com

Received: 25 April 2025; **Revised:** 24 November 2025; **Accepted:** 31 December 2025; **First published online:** 10 March 2026

Keywords: dish solar tracking platform; 3-RPS parallel manipulator; multi-objective optimization; genetic algorithm

Abstract

Under the backdrop of rapid advancements in renewable energy technologies and increasingly urgent demands for performance enhancement in solar power generation manipulator, this study proposes a three-revolute-prismatic-spherical (3-RPS) parallel manipulator featuring similar isosceles triangular moving and fixed platforms with revolute joint axes perpendicular to the angular bisectors of each vertex. Based on this manipulator, a novel dish solar concentrator was designed. Taking this concentrator as the research subject, kinematic analysis was conducted to derive the inverse kinematics model and overall Jacobian matrix of the manipulator. Three performance indexes were established: workspace, global motion/force transmission performance, and global stiffness performance. The Non-dominated Sorting Genetic Algorithm II genetic algorithm was applied for multi-objective optimization of the parallel manipulator, followed by TOPSIS decision-making based on the entropy weight method to select the optimal solution from the Pareto frontier. The distribution characteristics of these indexes within the achievable workspace before and after optimization were compared through performance atlas methodology. Static analyses were subsequently performed using finite element analysis to validate the manipulator's performance. Results demonstrate that the workspace index and global performance stiffness index achieved varying degrees of improvement, while the global motion/force transmission performance exhibited a slight overall decline. Nevertheless, under specific operational conditions, the optimized manipulator shows enhanced performance compared to the original design while strictly satisfying all constraint requirements.

1. Introduction

With the increasing depletion of fossil fuels and the escalating severity of associated environmental pollution, the transition to low-carbon energy structures has become imperative. Among various solar power technologies, dish solar thermal power generation demonstrates promising development prospects due to its unparalleled concentration efficiency and operational flexibility [1].

Enhancing solar thermal conversion efficiency fundamentally relies on solar tracking mechanisms that continuously adjust concentrator orientation to maintain optimal solar alignment throughout the day. Consequently, solar tracking systems constitute a critical component in dish-type solar thermal power plants. Current solar tracking technologies primarily fall into three categories: single-axis tracking, dual-axis tracking, and parallel mechanism-based tracking. While single-axis tracking systems offer structural simplicity, their unidirectional adjustment capability prevents concentrator axes from maintaining parallel alignment with solar rays [2, 3]. Dual-axis tracking parabolic dish systems enable bidirectional solar tracking, achieving year-round parallel alignment between concentrator axes and incident sunlight [4, 5]. Although these systems outperform single-axis configurations in energy harvesting efficiency, their end-effector drive mechanisms endure substantial payloads, exhibit error accumulation, and incur high maintenance costs [6, 7].

© The Author(s), 2026. Published by Cambridge University Press.

https://doi.org/10.1017/S0263574726103294 Published online by Cambridge University Press

To address these challenges, researchers have focused on parallel manipulators. Itul et al. [8] developed a simplified solar tracking system based on a 2-degree-of-freedom (DOF) parallel manipulator. However, structural limitations constrained its tracking range, preventing full hemispherical solar tracking. Shyam et al. [9, 10] proposed two centralized solar thermal power systems for central receiver towers using three-revolute-prismatic-spherical (3-RPS) and 3-universal-prismatic-universal (3-UPU) parallel manipulators, respectively. While these systems are suitable for large-scale solar plants, they overlooked the critical constraint of the parallel manipulator orientation workspace on tracking angular range. Sun et al. [11] designed a novel 6-DOF lightweight parallel manipulator with enhanced mobility, featuring large rotational range, compact structure, and hybrid translational-rotational motion capabilities, which satisfies the dual requirements of pointing and pose coordination in aerospace applications. Du et al. [2] further advanced this field by prototyping a solar tracker based on a U-PRU-PUS parallel manipulator with three kinematic limbs. Experimental validation confirmed its compliance with solar tracking performance specifications.

While ref. [12] introduced a dish solar tracking platform based on a 3-RPS parallel manipulator, its design overlooked the mass contribution of the Stirling engine, leading to potential performance limitations. To address this issue and enhance structural performance, this study relaxes the conventional equilateral triangular configuration constraint for both the moving and fixed platforms. Instead, similar isosceles triangular configurations with their apex angles oriented toward the manipulator center are proposed, aiming to achieve superior stiffness and payload capacity.

The design of a parallel manipulator generally involves dimensional optimization and control optimization. Dimensional optimization, typically conducted during the design phase, employs various methodologies such as genetic algorithms [13–15] and particle swarm optimization [16–18]. Given the complexity of multi-objective optimization solution sets, this research adopts hybrid approaches combining Technique for Order Preference by Similarity to Ideal Solution (TOPSIS) [19] and entropy weight method [20] to determine optimal solutions. This integrated methodology effectively minimizes subjective bias in decision-making while improving solution accuracy [21].

This study addresses the design and application requirements of solar tracking systems by defining a regular workspace index and further establishing global kinematic and stiffness performance indexes through the Jacobian matrix and stiffness matrix, respectively. Multiple objectives were simultaneously optimized using the Non-dominated Sorting Genetic Algorithm II (NSGA-II) algorithm to obtain the Pareto optimal frontier. Subsequently, the entropy weight method-based TOPSIS decision-making was employed to determine indicator weights, which guided the selection and validation of the optimal solution from the Pareto set.

2. Structural description and kinematic analysis

2.1. Geometrical description

While ref. [12] presented a 3-RPS parallel manipulator for dish solar tracking; its design neglected the mass contribution of the Stirling engine, potentially limiting rigidity and payload capacity. To overcome these constraints and enhance structural performance for solar tracking, this study modifies the conventional design: both platforms adopt geometrically similar isosceles triangles, rather than equilateral triangles, with apex angles oriented toward the manipulator center. This deliberate symmetry relaxation targets improved stiffness and payload capacity for precise sun-tracking under operational loads.

The dish solar tracking platform consists of a heat receiver, the support rods, the parabolic reflective mirror facets, the 3-RPS parallel tracking manipulators, and the racks, the structure of which is shown in Figure 1. Dual-layer parabolic mirrors, inner/outer, comprise identical mirror facets. The mirror facets are rigidly mounted to the backplate, serving as the moving platform of the 3-RPS parallel tracking manipulator, exhibiting congruent kinematic behavior with the platform, while the upper heat receiver is connected to the backplate via four support rods. All prismatic joints in the 3-RPS parallel tracking manipulator are equipped with three-stage hydraulic cylinders. By actively controlling the strokes of these hydraulic cylinders, the manipulator dynamically adjusts its pose to achieve precise solar tracking

https://doi.org/10.1017/S0263574726103294 Published online by Cambridge University Press

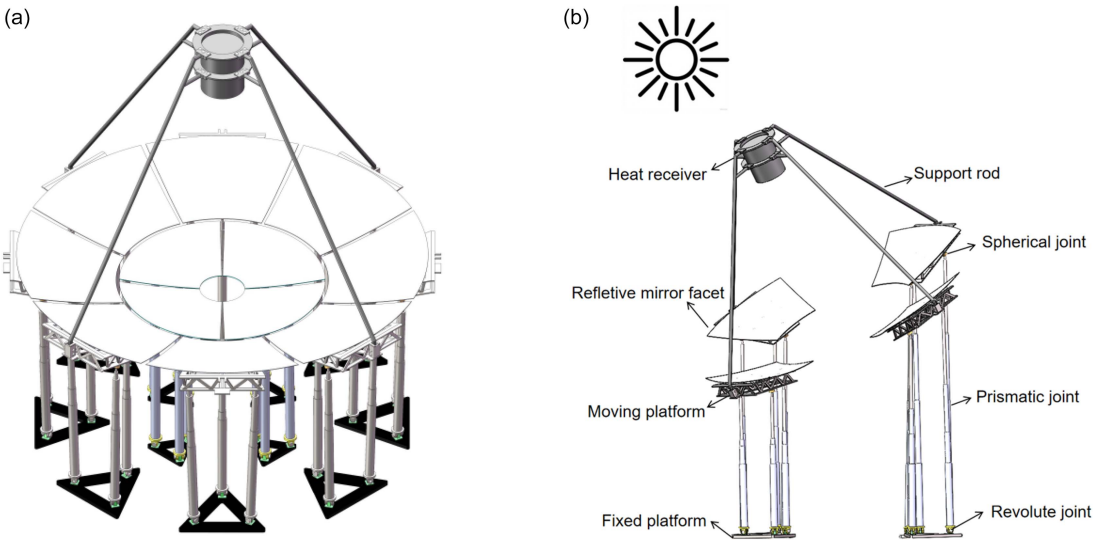


Figure 1. *Schematic diagrams of the parabolic dish solar tracking platform:(a) Overall structural schematic, (b) Solar-tracking support structural schematic.*

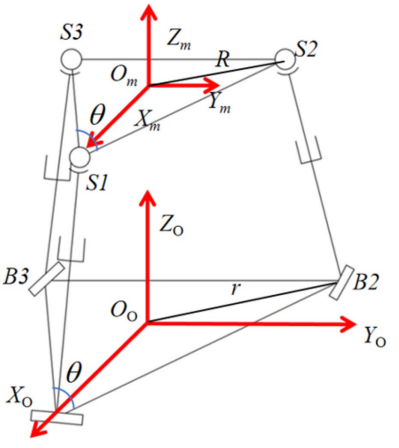


Figure 2. *Schematic diagram of the 3-RPS parallel manipulator.*

functionality. Appropriate inter-mirror clearances are maintained to prevent kinematic interference and mitigate wind load effects, while the heat receiver is precisely positioned at the parabolic focal point. The modular design enhances manufacturing, transportation, and assembly efficiency, with solar tracking functionality achieved through coordinated control of actuation systems. Subfigure (b) isolates the principal support 3-RPS parallel manipulators in the operating state with 30° elevation actuation.

2.2. Inverse kinematics analysis

The structural sketch of the 3-RPS parallel manipulator is shown in Figure 2, and the moving platform and the fixed platform adopt a similar isosceles triangle configuration.

Let the vertex of the moving platform be S_i, and the vertex of the fixed platform be B_i. Both platforms possess apex angles of equal magnitude θ, with the axes of the revolute joints being rigorously aligned along the angular bisector directions of their corresponding vertices. The circumradius of the moving platform and the fixed platform are R and r, respectively.

https://doi.org/10.1017/S0263574726103294 Published online by Cambridge University Press

The moving coordinate system $\{O_m\}$ is established with O_m, the circumcircle center of the moving platform, as its origin, where the X_m-axis passes through the center of spherical joint S_1, the Z_m-axis is vertically upward. The Y_m-axis follows the right-hand screw rule. Similarly, the fixed coordinate system $\{O_O\}$ is defined with O_O, the circumcircle center of the fixed platform, as its origin, where the X_O-axis is orthogonal to the revolute joint axis at B_1 and the Z_O-axis remains vertically oriented.

The attitude representation of the moving platform of this 3-RPS parallel manipulator adopts the Euler angle method and chooses the form of *Z-Y-X* around the moving axis. The rotation matrix in the form of *Z-Y-X* Euler angles is:

$$ {}^{O}\boldsymbol{R}_m = \begin{bmatrix} c\beta\, c\gamma & s\alpha s\beta\, c\gamma - s\gamma c\alpha & s\beta\, c\alpha c\gamma + s\alpha s\gamma \\ c\beta s\gamma & s\alpha s\beta s\gamma + c\alpha c\gamma & s\gamma s\beta\, c\alpha - s\alpha c\gamma \\ -s\beta & s\alpha c\beta & c\alpha c\beta \end{bmatrix} = \begin{bmatrix} n_1 & o_1 & a_1 \\ n_2 & o_2 & a_2 \\ n_3 & o_3 & a_3 \end{bmatrix} \tag{1} $$

where cos is abbreviated as c and sin is abbreviated as s. The sine and cosine functions appearing below are simplified similarly.

Set the initial position of the coordinate origin of the moving platform relative to the coordinate system of the fixed platform as $[0,\ 0,\ z]^T$, after three rotations of the coordinate axes the moving platform reaches a certain position and attitude, and its coordinates in the the fixed coordinate system is $[x_O,\ y_O,\ z_O]^T$, which remain equal for all limbs. According to the Euler angle form of the rotation matrix, it can be obtained that the coordinates of the three spherical joint centers of the moving platform are:

$$ \boldsymbol{S}_{Oi} = {}^{O}\boldsymbol{R}_m \cdot \boldsymbol{S}_{mi} + \begin{bmatrix} x_O \\ y_O \\ z_O \end{bmatrix} (i = 1, 2, 3) \tag{2} $$

where $\boldsymbol{S}_{mi}$ is the coordinates of the spherical joint centers in the moving coordinate system.

The first term on the right-hand side of Eq. (2) represents the rotational motion of the moving platform, while the second term corresponds to its translational motion. Consequently, the inverse kinematic model for the isosceles triangle-based 3-RPS parallel manipulator can be formulated as:

$$ L_i = \|\boldsymbol{S}_{Oi} - \boldsymbol{B}_{Oi}\| \ (i = 1, 2, 3) \tag{3} $$

where $\boldsymbol{B}_{oi}$ is the coordinates of the three revolute joints in the fixed coordinate system.

Combining simultaneously solving equations above yields:

$$ \begin{cases} L_1 = \sqrt{(Rn_1 + x_O - r)^2 + (Rn_2 + y_O)^2 + (Rn_3 + z_O)^2} \\ L_2 = \sqrt{(-Rn_1c\theta + Ro_1s\theta + x_O + rc\theta)^2 + (-Rn_2c\theta + Ro_2s\theta + y_O - rc\theta)^2 + (-Rn_3c\theta + Ro_3s\theta + z_O)^2} \\ L_3 = \sqrt{(-Rn_1c\theta + Ro_1s\theta + x_O + rc\theta)^2 + (-Rn_2c\theta + Ro_2s\theta + y_O + rc\theta)^2 + (-Rn_3c\theta + Ro_3s\theta + z_O)^2} \end{cases} \tag{4} $$

In the 3-RPS parallel manipulator, the three connecting rods are constrained to three distinct planes during motion due to restrictions imposed by revolute joints [22]. In the case of the 3-RPS parallel manipulator based on an isosceles triangle, these three planes intersect with the xoy-plane, with their lines of intersection being the perpendiculars to the angle bisectors of the isosceles triangle. This geometric relationship can be mathematically expressed as:

$$ \begin{cases} y_1 = 0 \\ y_2 = kx + kr\, c\theta + r\, s\theta \\ y_3 = kx + kr\, c\theta - r\, s\theta \end{cases} \tag{5} $$

where $k = \frac{1+s\frac{\theta}{2}}{c\frac{\theta}{2}}$

Substituting Eq. (2) into Eq. (5) yields:

$$ \begin{cases} Rn_2 + y_O = 0 \\ -Rn_2c\theta + Ro_2s\theta + y_O = kRn_1c\theta - kRo_1s\theta - kx_O - kr\, c\theta + r\, s\theta \\ -Rn_2c\theta - Ro_2s\theta + y_O = -kn_1Rc\theta - kRo_1s\theta + kx_O + kr\, c\theta - r\, s\theta \end{cases} \tag{6} $$

https://doi.org/10.1017/S0263574726103294 Published online by Cambridge University Press

After comparison and calculation, the constraint equation for the 3-RPS at this point can be written as:

$$\begin{cases} \gamma = \text{a tan } 2\left(s\frac{\theta}{2}s\alpha\ s\beta,\ c\beta\left(1-s\frac{\theta}{2}\right)+s\frac{\theta}{2}c\alpha\right) \\ x_O = c\theta\ (c\beta\ c\gamma - r) - 2s\frac{\theta}{2}\left(1-s\frac{\theta}{2}\right)(R\ s\alpha\ s\beta\ s\gamma + c\alpha\ c\gamma - r) \\ y_O = -R\ s\gamma\ c\beta \end{cases} \tag{7}$$

2.3. Construction of Jacobian matrix

From Figure 2, the following vector equation can be established.

$$\boldsymbol{O_O O_m} + \boldsymbol{O_m S_i} = \boldsymbol{O_O B_i} + \boldsymbol{B_i S_i} \tag{8}$$

Differentiating Eq. (8) with respect to time and rearranging the terms yields:

$$\boldsymbol{l_i} = \boldsymbol{n_{Li}}^T \cdot \boldsymbol{v_m} + (\boldsymbol{r_i} \times \boldsymbol{n_{Li}})^T \cdot \boldsymbol{\omega_m} \tag{9}$$

where $\boldsymbol{l_i}$ represents the velocity of the driving link in limb i, $\boldsymbol{n_{Li}}$ denotes the unit vector along the axis of each actuator rod, $\boldsymbol{v_m}$ and $\boldsymbol{\omega_m}$, respectively, denote the linear velocity and angular velocity of the moving platform center, and $\boldsymbol{r_i}$ refers to the position vector from $\boldsymbol{O_m}$ to $\boldsymbol{S_i}$.

Organizing the equations for each limbs into matrix form can be expressed as:

$$\begin{bmatrix} \boldsymbol{l_1} \\ \boldsymbol{l_2} \\ \boldsymbol{l_3} \end{bmatrix} = \begin{bmatrix} \boldsymbol{n_{L1}}^T & (\boldsymbol{r_1} \times \boldsymbol{n_{L1}})^T \\ \boldsymbol{n_{L2}}^T & (\boldsymbol{r_2} \times \boldsymbol{n_{L2}})^T \\ \boldsymbol{n_{L3}}^T & (\boldsymbol{r_3} \times \boldsymbol{n_{L3}})^T \end{bmatrix} \cdot \begin{bmatrix} \boldsymbol{v_m} \\ \boldsymbol{\omega_m} \end{bmatrix} \tag{10}$$

The kinematic Jacobian matrix of the 3-RPS parallel manipulator can be formulated as:

$$\boldsymbol{J_m} = \left(\boldsymbol{n_{Li}}^T\ (\boldsymbol{r_i} \times \boldsymbol{n_{Li}})^T\right) \tag{11}$$

The spherical joint is a 3-DOF kinematic joint, while all others are single-DOF kinematic joints. As analyzed through screw theory, the motion screw system of a single limb i contains five joint screws, which can be expressed as:

$$\begin{cases} \$_{1i} = \left[\boldsymbol{n_{bi}}^T; (\boldsymbol{O_O B_i} \times \boldsymbol{n_{bi}})^T\right] \\ \$_{2i} = \left[\boldsymbol{0}_{1\times 3}; \boldsymbol{n_{Li}}^T\right] \\ \$_{3i} = \left[\boldsymbol{S_{3i}}^T; (\boldsymbol{O_O P_i} \times \boldsymbol{S_{3i}})^T\right] \\ \$_{4i} = \left[\boldsymbol{S_{4i}}^T; (\boldsymbol{O_O P_i} \times \boldsymbol{S_{4i}})^T\right] \\ \$_{5i} = \left[\boldsymbol{S_{5i}}^T; (\boldsymbol{O_O P_i} \times \boldsymbol{S_{5i}})^T\right] \end{cases} \tag{12}$$

where $\boldsymbol{n_{bi}}$ denotes the unit vector along the axis of the revolute joint in limb i, $\boldsymbol{S_{3i}} = [1, 0, 0]^T$; $\boldsymbol{S_{4i}} = [0, 1, 0]^T$; $\boldsymbol{S_{5i}} = [0, 0, 1]^T$.

In screw theory, since the reciprocal product between the constraint wrench screw and the system of motion screw equals zero, the constraint wrench screw can be expressed as:

$$\$_{Ci} = \left[\boldsymbol{n_{bi}}^T; (\boldsymbol{r_i} \times \boldsymbol{n_{bi}})^T\right] \tag{13}$$

The velocity of the moving platform center can be expressed as:

$$\$_m = [\boldsymbol{v_m}; \boldsymbol{\omega_m}] \tag{14}$$

The reciprocal product of Eqs. (13) and (14) yields:

$$\$_{Ci} \circ \$_m = 0 \tag{15}$$

https://doi.org/10.1017/S0263574726103294 Published online by Cambridge University Press

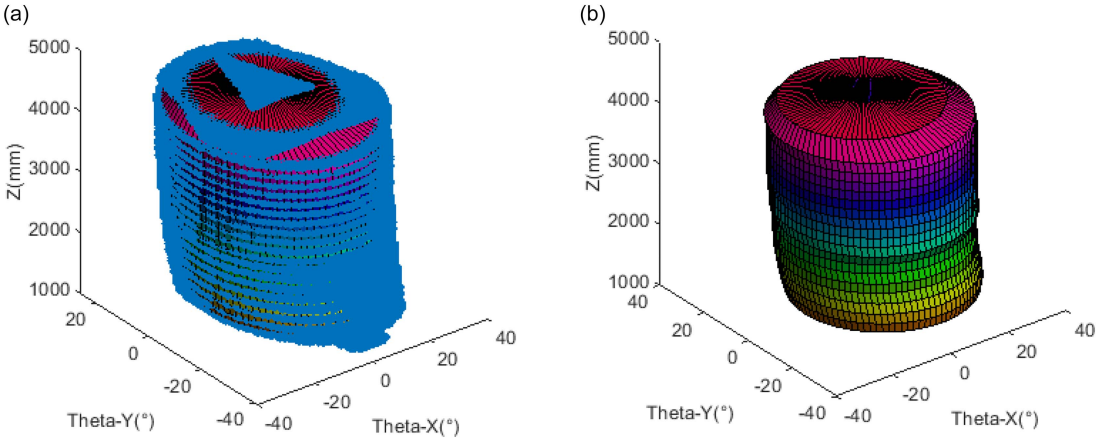


Figure 3. *Workspace of 3-RPS parallel manipulator: (a) Combined visualizationof reachable workspace points (blue) and regular workspace, (b) Pure regular workspace.*

Rearranging into matrix form yields:

$$\boldsymbol{J}_C \cdot \begin{bmatrix} \boldsymbol{v}_m \\ \boldsymbol{\omega}_m \end{bmatrix} = 0, \quad \boldsymbol{J}_C = \begin{bmatrix} \boldsymbol{n}_{b1}{}^T & (\boldsymbol{r}_1 \times \boldsymbol{n}_{b1})^T \\ \boldsymbol{n}_{b2}{}^T & (\boldsymbol{r}_2 \times \boldsymbol{n}_{b2})^T \\ \boldsymbol{n}_{b3}{}^T & (\boldsymbol{r}_3 \times \boldsymbol{n}_{b3})^T \end{bmatrix} \tag{16}$$

where $\boldsymbol{J}_C$ denotes the constraint Jacobian matrix of the manipulator.

The overall Jacobian matrix can be obtained by combining Eqs. (11) and (16).

$$\begin{bmatrix} \boldsymbol{l}_i \\ 0 \end{bmatrix}_{6\times 1} = \begin{bmatrix} \boldsymbol{J}_m \\ \boldsymbol{J}_C \end{bmatrix} \cdot \begin{bmatrix} \boldsymbol{v}_m \\ \boldsymbol{\omega}_m \end{bmatrix}, \boldsymbol{J} = \begin{bmatrix} \boldsymbol{J}_m \\ \boldsymbol{J}_C \end{bmatrix} \tag{17}$$

$\boldsymbol{J}$ is the overall Jacobian matrix for the organization.

3. Performance indices

The multi-objective optimization system integrates practical requirements to construct global performance indices. For comprehensive optimization, local objective functions must be combined into globally representative composite functions. The workspace serves both as a core optimization target and the foundation for formulating these global objectives. This section details three globally defined functions capturing holistic manipulator performance.

3.1. Workspace index

The regular workspace, defined by its shape and size, constitutes a critical performance index for parallel manipulators and serves as an essential optimization objective function. This study employs a polar coordinate methodology involving three key phases: First, the shape of the reachable workspace is determined using a spatial search method. Subsequently, the operational platform's vertical displacement is discretized into multiple equidistant layers [23], with each layer's maximum inscribed circle radius calculated through convex hull analysis. These derived maximum radii enable volumetric computation of a standardized cylindrical or truncated conical workspace, as illustrated in Figure 3.

The workspace of the 3-RPS parallel manipulator can be formulated as:

$$V_r = \sum_{i=1}^{n-1} \frac{1}{2} (A_i + A_{i+1}) * \Delta z \tag{18}$$

https://doi.org/10.1017/S0263574726103294 Published online by Cambridge University Press

where A_i denotes the radius of the maximum inscribed circle of each layer, Δz represents the height interval.

3.2. Kinematic performance index

The condition number of the Jacobian matrix remains one of the most widely used kinematic indexes [24]. However, its primary deficiency lies in dimensional inhomogeneity and coordinate dependency, resulting in inconsistent units and ambiguous physical interpretation of the Jacobian matrix, an issue particularly pronounced in hybrid-DOF manipulators. This study adopts the motion/force transmission performance index proposed by Wang et al. [25], which evaluates the energy transmission efficiency from inputs to outputs in parallel manipulators. Its main advantage is that it is a dimensionless index with values ranging from 0 to 1, independent of the coordinate system, where values approaching 1 indicate manipulators nearing optimal energy transmission configurations.

For the 3-RPS parallel manipulator, since the actuated joint in each limb is a prismatic joint and exhibits pure translation, the input twist screw can be expressed as:

$$\$_{Ii} = \left[\boldsymbol{0}_{1\times 3};\quad \boldsymbol{n}_{Li}{}^{T}\right] \tag{19}$$

Therefore, since the reciprocal product between the transmission wrench screw $\$_{Ti}$ and the remaining screws in the motion screw system after removing the driving force screw equals zero, leading to:

$$\$_{Ti} = \left[\boldsymbol{n}_{Li}{}^{T};\ (\boldsymbol{r}_i \times \boldsymbol{n}_{Li})^{T}\right] \tag{20}$$

Therefore, the input transmission index of the limb i is:

$$\lambda_i = \frac{\left|\$_{Ti} \circ \$_{Ii}\right|}{\left|\$_{Ti} \circ \$_{Ii}\right|_{\max}} = \left|\boldsymbol{n}_{Li}{}^{T} \times \boldsymbol{n}_{Li}{}^{T}\right| = 1 \tag{21}$$

When all actuated joints except those in limb i are locked, the transmission force screw in limb j transforms into a constraint screw ($i, j = 1, 2, 3; i \neq j$). Consequently, the constraint wrench screw system of the manipulator becomes:

$$\boldsymbol{U}_i = \left\{\$_{Tj}, \$_{Tk}, \$_{Ci}, \$_{C2}, \$_{C3}\right\}\ (j \neq k; j, k \neq i) \tag{22}$$

In this case, the manipulator is a single-DOF manipulator, and the instantaneous motion of the moving platform can be expressed by the output twist screw, which can be obtained by the reciprocal product with the constraint wrench screw system U_i equal to zero.

$$\$_{Oi} \circ \boldsymbol{U}_i = 0 \tag{23}$$

Thus, the output transmission index for limb i is:

$$\eta_i = \frac{\left|\$_{Ti} \circ \$_{Oi}\right|}{\left|\$_{Ti} \circ \$_{Oi}\right|_{\max}} \tag{24}$$

Considering both input and output transmission index, local motion/force transmission index *LTI* is defined as follows:

$$LTI = \min\{\lambda_i, \eta_i\} = \eta_i \tag{25}$$

Define the global motion/force transmission index (*GTI*) to evaluate the kinematic performance index of the manipulator in the complete workspace, expressed as:

$$GTI = \frac{\int_{V_r} LTI dV_r}{\int_{V_r} dV_r} \tag{26}$$

https://doi.org/10.1017/S0263574726103294 Published online by Cambridge University Press

3.3. Stiffness performance index

This section uses the virtual joint method (VJM) to establish the stiffness model. Each limb is modeled as a serial chain with elastic elements and passive joints. In this approach, revolute joints and spherical joints are treated as ideal passive joints. The model is built by first determining individual limb stiffness and then aggregating them into the overall mechanism stiffness matrix.

Each RPS limb can be modeled as a serial chain with passive joints, and the kinematic model can be rewritten in the form of a vector function [26]:

$$\boldsymbol{t} = \boldsymbol{g}\,(\boldsymbol{q},\ \ \boldsymbol{\theta}) \tag{27}$$

where $\boldsymbol{t} = [\,x \quad y \quad z \quad \phi_x \quad \phi_y \quad \phi_z\,]^T$ denotes the pose of the end-effector in the Cartesian space for a single RPS kinematic chain. The first three components represent the positional coordinates, while the latter three define the orientation.

Let the coordinates of the trivial passive joints and virtual joints be denoted as $\boldsymbol{q} = (\,q_1, \quad q_2, \quad q_3\,)^T$ and $\boldsymbol{\theta} = (\,\theta_1, \quad \theta_2, \quad \theta_3\,)^T$.

Let the initial state be denoted as $\boldsymbol{t}_0 = \boldsymbol{g}(\boldsymbol{q}_0, 0)$, where $\boldsymbol{q}_0$ is computed via inverse kinematics. Then, the relationship between the end-effector's small displacement Δt and the variations in joint variables can be expressed as:

$$\Delta \boldsymbol{t} = \boldsymbol{t}_0 + \boldsymbol{J}_\theta \Delta \boldsymbol{\theta} + \boldsymbol{J}_q \Delta \boldsymbol{q} \tag{28}$$

where $\boldsymbol{J}_\theta = \frac{\partial \boldsymbol{g}}{\partial \boldsymbol{\theta}}$ and $\boldsymbol{J}_q = \frac{\partial \boldsymbol{g}}{\partial \boldsymbol{q}}$ denote the Jacobian matrices corresponding to the virtual joints and the passive joints.

Based on the principle of virtual work, the system is in a state of static equilibrium when the end-effector is subjected to an external force/moment vector $\boldsymbol{F}$. In this state, the equivalent force / moment vector in the virtual joints $\boldsymbol{\tau}_\theta$, and the constraint force/moment vector in the passive joints $\boldsymbol{\tau}_q$, satisfy the following equilibrium condition:

$$\begin{cases} \boldsymbol{J}_\theta{}^T \cdot \boldsymbol{F} = \boldsymbol{\tau}_\theta \\ \boldsymbol{J}_q{}^T \cdot \boldsymbol{F} = \boldsymbol{\tau}_q = \boldsymbol{0} \end{cases} \tag{29}$$

The mechanical behavior of the virtual joints is governed by their elastic properties; the force-deformation relationship follows Hooke's law and can be expressed as:

$$\boldsymbol{\tau}_\theta = \boldsymbol{K}_\theta \cdot \boldsymbol{\theta} \tag{30}$$

where $\boldsymbol{K}_\theta$ is the stiffness matrix of the virtual spring, which is a positive definite diagonal matrix whose elements are determined by the physical parameters of the links.

By combining the equation $\Delta \boldsymbol{t} = \boldsymbol{t}_0 + \boldsymbol{J}_\theta \Delta \boldsymbol{\theta} + \boldsymbol{J}_q \Delta \boldsymbol{q}$ with the equilibrium equations and physical relationships mentioned above, it can be represented in the matrix form as follows [27]:

$$\begin{bmatrix} 0 & \boldsymbol{J}_\theta & \boldsymbol{J}_q \\ \boldsymbol{J}_\theta^T & -\boldsymbol{K}_\theta & 0 \\ \boldsymbol{J}_q^T & 0 & 0 \end{bmatrix} \cdot \begin{bmatrix} \boldsymbol{F} \\ \theta \\ \Delta \boldsymbol{q} \end{bmatrix} = \begin{bmatrix} \Delta \boldsymbol{t} \\ 0 \\ 0 \end{bmatrix} \tag{31}$$

By performing an inversion of this coefficient matrix and extracting its upper-left 6×6 sub-matrix, the Cartesian stiffness matrix of the kinematic chain $\boldsymbol{K}_C$ at the end-effector point can be obtained as:

$$\begin{bmatrix} \boldsymbol{J}_\theta \cdot \boldsymbol{K}_\theta^{-1} \cdot \boldsymbol{J}_\theta^T & \boldsymbol{J}_q \\ \boldsymbol{J}_q^T & 0 \end{bmatrix}^{-1} = \begin{bmatrix} \boldsymbol{K}_C & * \\ * & * \end{bmatrix} \tag{32}$$

After obtaining the Cartesian stiffness matrices $\boldsymbol{K}_C^{(i)}$ for each kinematic chain i, it is necessary to aggregate them to establish the overall model. For this purpose, the stiffness matrix of each chain $\boldsymbol{K}_C^{(i)}$ must be transformed to the unified reference point $\boldsymbol{O}_{\mathrm{O}}$ of the fixed platform. Finally, the global stiffness matrix of the 3-RPS mechanism can be obtained by the following expression.

$$\boldsymbol{K}_{C,O} = \sum_{i=1}^{3} \boldsymbol{K}_{C,O}^{(i)} \tag{33}$$

https://doi.org/10.1017/S0263574726103294 Published online by Cambridge University Press

The Local Stiffness Index (*LSI*), defined as the minimum singular value of the stiffness matrix, provides a quantitative evaluation of the parallel manipulator's rigidity at a given configuration.

$$LSI = \sigma_{\min}\left(\boldsymbol{K}_{C,O}\right) \tag{34}$$

At any pose, *LSI* exhibits a strictly monotonic positive correlation with stiffness performance: higher values indicate superior load-bearing capacity and reduced deformation [25].

However, the local stiffness performance index fails to reflect stiffness variation trends when the manipulator alters its configuration. To address this deficiency, the global stiffness performance index (*GSI*), which incorporates the average stiffness over the reachable workspace, is introduced. The *GSI* is mathematically defined as:

$$GSI = \frac{\int_{V_r} LSI dV_r}{\int_{V_r} dV_r} \tag{35}$$

4. Multi-objective optimization

In parallel manipulator design, single-objective optimization often fails to address multidimensional performance requirements. Thus, a multi-objective method is adopted to balance competing goals for global optimization. This chapter establishes the optimization framework with design variables and constraints, details the multi-objective approach, and selects optimal solutions validated by comparative studies and finite element analysis.

4.1. Establishment of optimization model

Based on the regular workspace constructed in Chapter 3, with *GTI* and *GSI* serving as objective functions, the workspace volume V_r by is multiplied a factor of 10^{-3} to maintain all objective function values within the same order of magnitude. The circumradius R of the moving platform, the ratio k_r of circumradii between the moving and fixed platforms, and the apex angles θ of both platforms are selected as optimization variables. The manipulator's motion is primarily constrained by three key factors: the limb motion strokes, the rotation angle ranges of revolute joints, and the angular ranges of spherical joints.

The mathematical model of multi-objective optimization can be expressed as:

$$\begin{aligned} \min_{R,k_r,\theta} \boldsymbol{F} &= \left[-10^{-3}V,\ -GTI,\ -GSI\right]^T \\ s.t \quad & 560mm \le R \le 1040mm \\ & 0.75 \le k_r \le 2 \\ & 50^\circ \le \theta \le 120^\circ \\ & L_{\min} \le L_i \le L_{\max} \\ & |\vartheta_{Bi}| \le 120^\circ \\ & |\vartheta_{Si}| \le 60^\circ \end{aligned} \tag{36}$$

where $L_{\min} = 1250mm$ and $L_{\max} = 4500mm$ denote the minimum and maximum limit lengths of the limbs, ϑ_{Si} and ϑ_{Bi} represent the angular ranges of the spherical joints and revolute joints for each limb.

4.2. Optimization method

This study employs the NSGA-II proposed in ref. [28] as the optimization method, whose procedure is illustrated in Figure 4. The core procedure of the genetic algorithm comprises four fundamental stages:

1. Population initialization: At iteration $t = 1$, randomly generate N solutions to form the initial population P_1. Evaluate the domination count and crowding distance of each solution.
2. Crossover, mutation, and evaluation: Generate offspring population Q_t through crossover operations. Apply mutation operations to individuals in the offspring population with a specified

https://doi.org/10.1017/S0263574726103294 Published online by Cambridge University Press

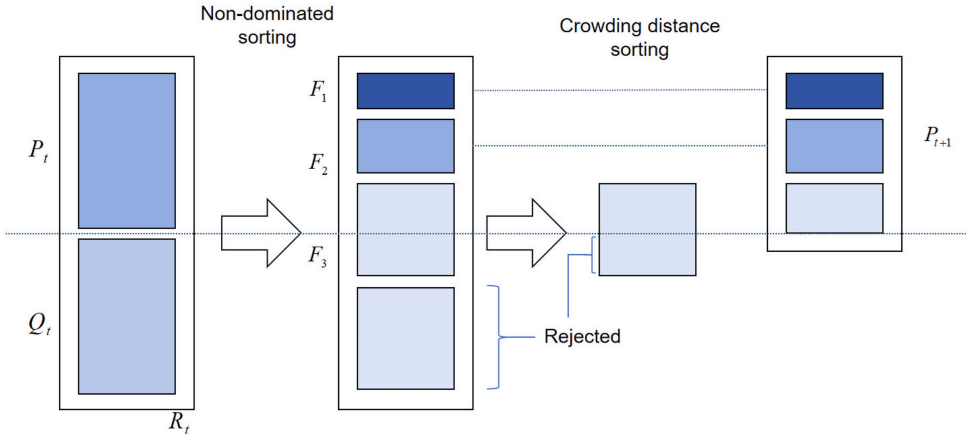


Figure 4. *NSGA-II procedure.*

mutation probability. Subsequently, evaluate the fitness values of all solutions in the offspring population Q_t.

3. Population selection: Select N high-quality individuals from the combined parent-offspring population Q_t to form the next-generation population P_{t+1}.
4. Termination criterion: If the maximum number of iterations is reached, terminate the algorithm and output the optimization results.

NSGA-II advances conventional genetic algorithms by integrating elitist preservation with non-dominated sorting. Its crowding distance operator quantifies solution distribution uniformity, achieving computational efficiency while preserving diversity. The workflow initiates by merging parent and offspring populations into an elite candidate pool. Subsequent fast non-dominated sorting stratifies solutions into mutually exclusive frontier layers, with strict precedence given to the optimal frontier. Where solution tiers exceed population capacity, secondary screening activates via crowding distance metrics. This cascaded approach maintains controlled computational loads while dynamically balancing convergence precision and distribution uniformity.

4.3. Optimization results selection and analysis

While NSGA-II produces a Pareto solution set spanning broad performance ranges, practical problems require a single optimal solution. Thus, the entropy-weighted TOPSIS model is employed. This method objectively weights evaluation criteria and calculates each solution's closeness to the ideal point, enabling relative ranking. The optimal trade-off solution is thereby identified within the Pareto frontier.

Define a decision matrix as:

$$\boldsymbol{D} = \begin{bmatrix} d_{11} & d_{12} & \cdots & d_{1m} \\ d_{21} & d_{22} & \cdots & d_{2m} \\ d_{31} & d_{32} & \cdots & d_{3m} \end{bmatrix} \tag{37}$$

where d_{ij} denotes the value of the criterion i for the alternative j, and m represents the total number of alternatives.

The decision matrix is normalized by:

$$r_{ij} = \frac{d_{ij}}{\sqrt{\sum_{j=1}^{m} d_{ij}}} \tag{38}$$

The process of obtaining weights by the entropy weighting method also requires standardized data, and since this NSGA-II algorithm uses all positive indicators, the data standardization step of the entropy

https://doi.org/10.1017/S0263574726103294 Published online by Cambridge University Press

Table I. *The original and optimized manipulator parameters and performance indexes.*

	$R(mm)$	k_r	$\theta(^\circ)$	$V_r(10^{-3}mm^3)$	GTI	GSI
Original	800	1.5	60	6.153	0.544	0.739
Optimized	560	1.154	66.135	7.851	0.535	0.817

weighting method is simplified as:

$$n_{ij} = \frac{d_{ij} - \min(d_{ij})}{\max(d_{ij}) - \min(d_{ij})} \tag{39}$$

Define the probability matrix as:

$$p_{ij} = \frac{n_{ij}}{\sum_{j=1}^{m} n_{ij}} \tag{40}$$

The information entropy of each index is obtained through the following equation.

$$e_i = -\ln(m)^{-1} \sum_{i=1}^{3} p_{ij} \ln p_{ij} \tag{41}$$

Entropy weights is obtained by:

$$w_i = \frac{1 - e_i}{\sum_{i=1}^{3} (1 - e_i)} \tag{42}$$

The decision matrix is obtained from the following equation:

$$v_{ij} = w_i \times r_{ij} \tag{43}$$

The positive and negative ideal solutions are determined through the following calculations:

$$\begin{aligned} A^+ &= \left\{ \max(v_{1m}), \quad \max(v_{2m}), \quad \max(v_{3m}) \right\} \\ A^- &= \left\{ \min(v_{1m}), \quad \min(v_{2m}), \quad \min(v_{3m}) \right\} \end{aligned} \tag{44}$$

Calculating the positive and negative ideal solutions by:

$$\begin{aligned} S^+ &= \sqrt{\sum_{j=1}^{m} \left(v_{ij} - A_j^+\right)^2} \\ S^- &= \sqrt{\sum_{j=1}^{m} \left(v_{ij} - A_j^-\right)^2} \end{aligned} \tag{45}$$

Define C_j relative closeness as follows, indicating how close the scheme is to the ideal solution.

$$C_j = \frac{S^+}{S^+ + S^-} \tag{46}$$

The value of C_j is in the range of $[0, 1]$, with larger values indicating better overall alternatives performance.

The solution ultimately selected from the Pareto solution set through entropy weight method-based TOPSIS decision-making is compared with the original dimensional parameters and performance indexes in Table 1. Comparative analysis demonstrates that the optimized manipulator exhibits a 27.60% enhancement in regular workspace index V_r, a 1.65% reduction in global motion/force transmission performance index GTI, and a 10.55% improvement in GSI.

Figure 5 presents local motion/force transmission index LTI across all feasible configurations for both original and optimized designs. The analysis reveals that while maintaining comparable median values, the optimized manipulator surpasses the original performance thresholds under specific operational conditions, achieving enhanced kinematic characteristics. This finding indicates the optimization strategy effectively exploits the latent capabilities of the 3-RPS parallel manipulator. Although reduced

https://doi.org/10.1017/S0263574726103294 Published online by Cambridge University Press

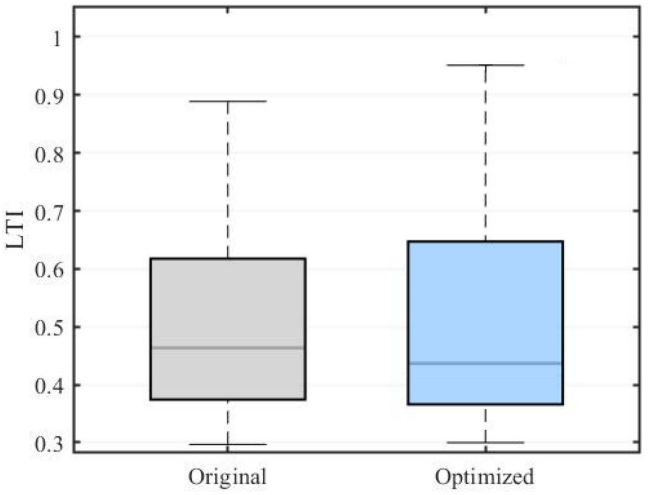


Figure 5. *Boxplot of LTI across spatially feasible points before and after optimization.*

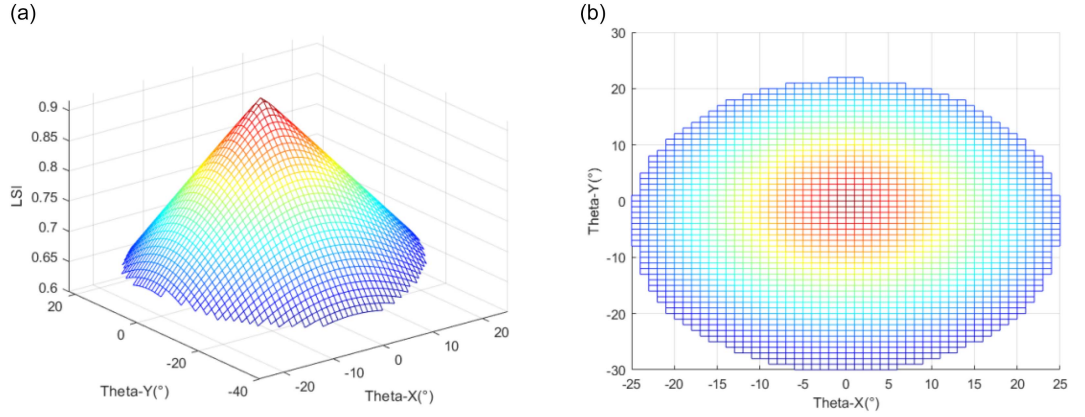


Figure 6. *LSI atlas of original design: (a) Volumetric distribution, (b) In-plane projection on XY coordinates.*

kinematic performance occurs in partial working modes, all operational states strictly satisfy prescribed design constraints.

As illustrated in Figures 6 and 7, the local stiffness performance index *LSI* exhibits symmetry with respect to the deflection angle about the *y*-axis, where the optimized manipulator demonstrates enhanced stiffness compared to the original configuration.

The local motion/force transmission index *LTI* at all feasible points before and after optimization at the same height of the manipulator are calculated by Eq. (24) and plotted as contour plots as shown in Figure 8. From the figure, it can be seen that for the indexes at the same height, although the maximum value and the distribution after optimization decreased compared with the optimized design, the sub-optimal values account for a higher proportion and better distribution.

To further validate the effectiveness of the manipulator optimization, this study developed a static finite element model on the ANSYS Workbench platform to simulate deformation responses under self-weight loads. Comparative evaluations of total deformation magnitudes and equivalent stress distributions between original and optimized configurations were conducted to assess multi-objective optimization effectiveness. Since each mirror facet is independently supported by a 3-RPS parallel manipulator, finite element analysis was specifically performed on the four 3-RPS parallel manipulators responsible for supporting the heat receiver. The resultant total deformation contour plots for both

https://doi.org/10.1017/S0263574726103294 Published online by Cambridge University Press

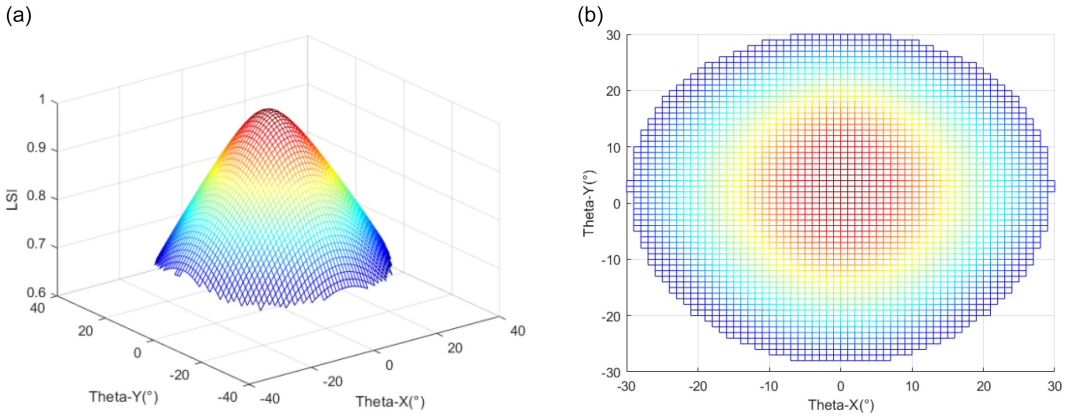


Figure 7. *LSI atlas of optimized design: (a) Volumetric distribution, (b) In-plane projection on XY coordinates.*

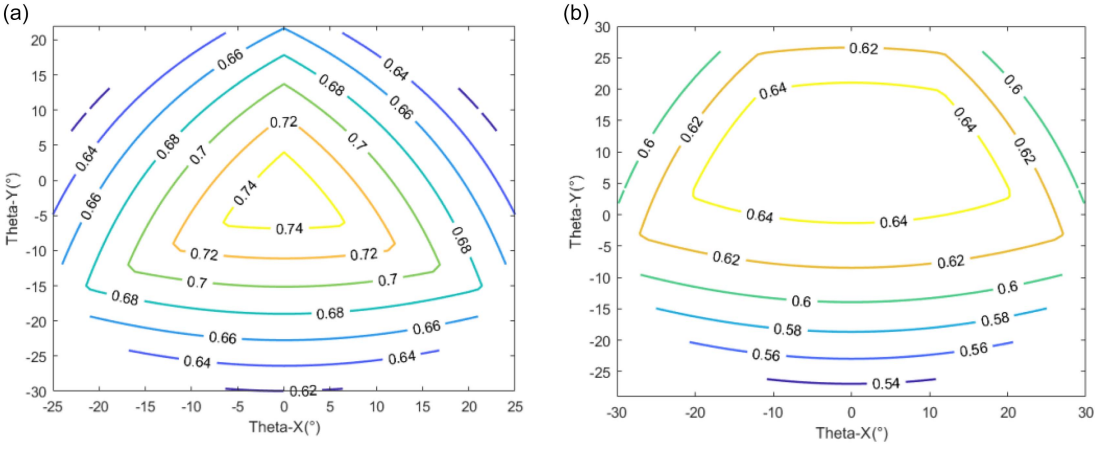


Figure 8. *Contour map of LTI at a specific height: (a) Original, (b) optimized.*

original and optimized configurations are presented in Figures 9 and 10, while the equivalent stress contour plots for both original and optimized configurations are shown in Figure 11.

Analysis of Figures 9, 10, and 11 reveals that under self-weight loading conditions, the original configuration sustains a maximum stress of 121.86 MPa with 5.128 mm deformation, while the optimized manipulator exhibits reduced maximum stress to 94.675 MPa and reduced deformation to 4.2404 mm. These original and optimized configurations comparisons demonstrate marked improvements in both equivalent stress distribution and deformation, thus confirming enhanced stiffness performance in the optimized 3-RPS parallel tracking manipulator.

5. Conclusions

This paper proposes a 3-RPS parallel solar tracking manipulator with isosceles-triangular platforms, relaxing symmetry constraints to enhance structural stiffness and surpass conventional equilateral design limitations. The NSGA-II algorithm obtains an optimized Pareto solution set for the manipulator, from which the optimal solution is selected via entropy-weighted TOPSIS decision-making. Results indicate a 27.60% improvement in workspace index, a 10.55% enhancement in global stiffness index, and a 1.65% reduction in GTI. Although overall motion/force performance remains consistent, specific operational conditions demonstrate measurable improvements over the original design while strictly satisfying all

https://doi.org/10.1017/S0263574726103294 Published online by Cambridge University Press

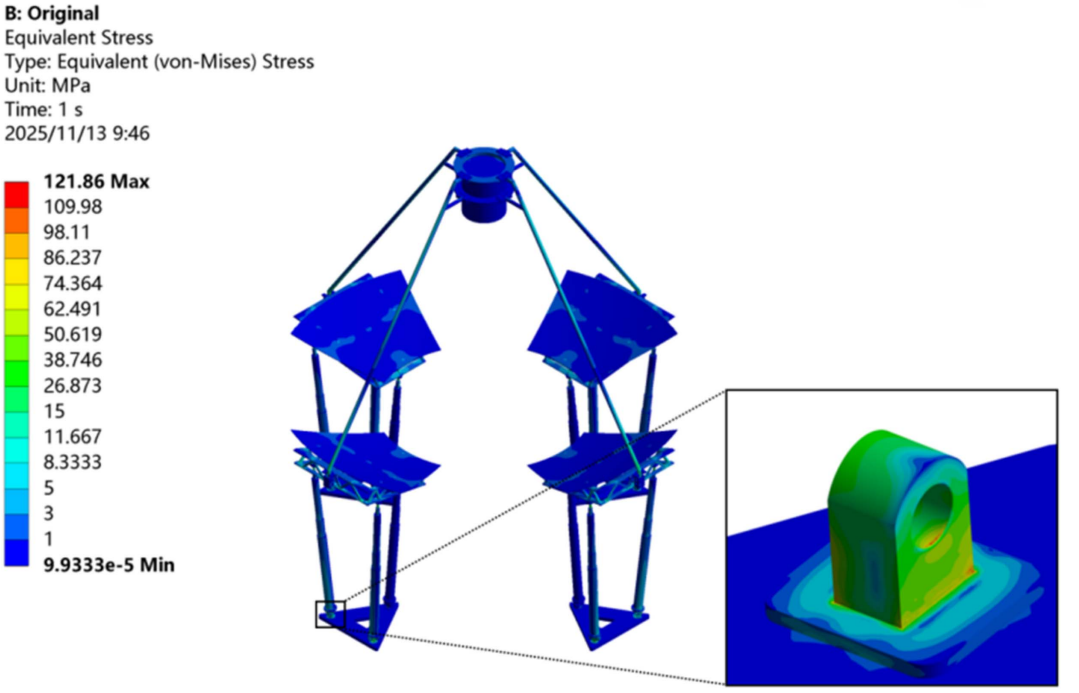


Figure 9. *Total deformation contour plots of the original manipulator.*

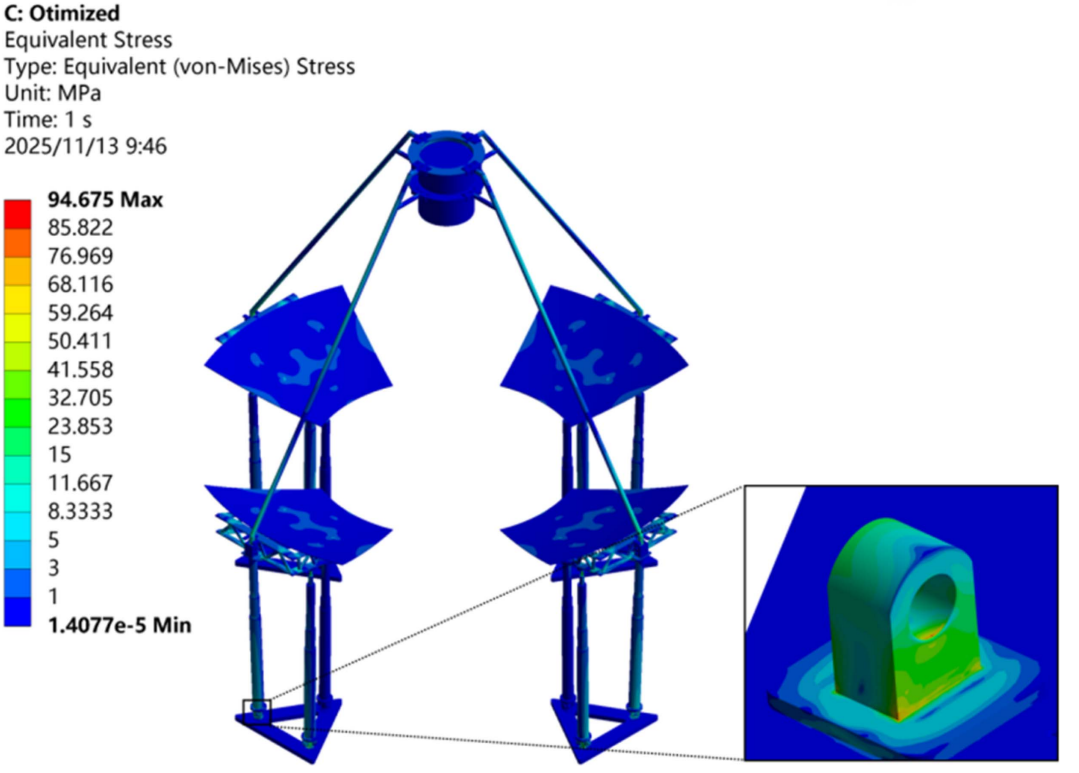


Figure 10. *Total deformation contour plots of the optimized manipulator.*

https://doi.org/10.1017/S0263574726103294 Published online by Cambridge University Press

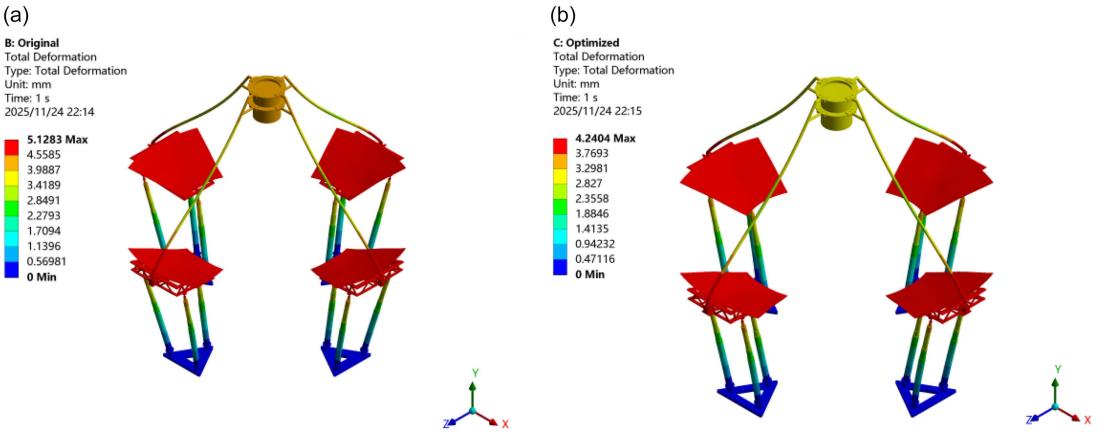


Figure 11. *Equivalent stress contour plots: (a) Original (130x scale), (b) optimized(140x scale).*

constraints. Comparative pre/post-optimization metrics and finite element analysis confirm enhanced stiffness and workspace capabilities in the optimized isosceles-configuration manipulator.

Author contribution. The study was initiated by Fanmao Liu and Shen Yao. Shen Yao was responsible for the overall design of the optimization framework, performing the majority of the simulations and data analysis, and writing the initial draft. Han Mo assisted in the validation of the simulation model. Hanlin Gong helped with the literature review and data visualization. Yunlong Chen and Tao Yang contributed to preparing the figures. All authors discussed the results, commented on, and revised the manuscript.

Financial support. This research received no specific grant from any funding agency, commercial, or not-for-profit sectors.

Competing interests. The authors declare no competing interests exist.

Ethical standards. Not applicable.

References

[1] M. H. Ahmadi, M. Ghazvini, M. Sadeghzadeh, M. Alhuyi Nazari, R. Kumar, A. Naeimi and T. Ming, "Solar power technology for electricity generation: A critical review," *Energy Sci. Eng.* **6**(5), 340–361 (2018).
[2] X. Du, Y. Li, P. Wang, Z. Ma, D. Li and C. Wu, "Design and optimization of solar tracker with U-PRU-PUS parallel mechanism," *Mech. Mach. Theory* **155**, 104107 (2021).
[3] A. A. Elsayed, E. E. Khalil, M. A. Kassem and O. A. Huzzayin, "A novel mechanical solar tracking mechanism with single axis of tracking for develo** countries," *Renew. Energy* **1**(170), 1129–1142 (2021).
[4] Y. Bian, B. Zhu, J. Wu and T. Y. Forward. "Inverse Kinematics and Optimal Design of a Parallel Solar Tracker," **In**: 2024 9th International Conference on Automation, Control and Robotics Engineering (CACRE) (IEEE, 2024), 382–388.
[5] K. Kumba, P. Upender, P. Buduma, M. Sarkar, S. P. Simon and V. Gundu, "Solar tracking systems: Advancements, challenges, and future directions: A review," *Energy Rep.* **1**(12), 3566–3583 (2024).
[6] C. Alexandru, "Simulation and optimization of a dual-axis solar tracking mechanism," *Mathematics* **12**(7), 1034 (2024).
[7] S. K. Natarajan, V. Thampi, R. Shaw, V. S. Kumar, R. S. Nandu, V. Jayan, N. Rajagopalan and R. K. Kandasamy, "Experimental analysis of a two-axis tracking system for solar parabolic dish collector," *Int. J. Energy Res.* **43**(2), 1012–1018 (2019).
[8] T. Itul, D. Pisla and A. Stoica, "Kinematics and Design of a Simple 2-DOF Parallel Mechanism Used for Orientation," **In**: *New Trends in Mechanism Science: Analysis and Design* (Springer Netherlands, 2010), pp. 39–46.
[9] R. A. Shyam, M. Acharya and A. Ghosal, "A heliostat based on a three degree-of-freedom parallel manipulator," *Solar Energy* **157**, 672–686 (2017).
[10] R. A. Shyam and A. Ghosal, "Path planning of a 3-UPU wrist manipulator for sun tracking in central receiver tower systems," *Mech. Mach. Theory* **119**, 130–141 (2018).
[11] J. Sun, L. Shao, L. Fu, X. Han and S. Li, "Kinematic analysis and optimal design of a novel parallel pointing mechanism," *Aerosp. Sci. Technol.* **104**, 105931 (2020).
[12] H. Mo, F. Liu, C. Liao and Y. Zhang, "Design, modeling and solar tracking control for a novel parabolic dish solar concentrator," *Robotica* **41**(10), 2985–3003 (2023).

https://doi.org/10.1017/S0263574726103294 Published online by Cambridge University Press

[13] J. Zhao, C. Wu, G. Yang, C. Y. Chen, S. Chen, C. ong and C. Zhang, "Kinematics analysis and workspace optimization for a 4-DOF. 3T1R parallel manipulator," *Mech. Mach. Theory* **167**, 104484 (2022).
[14] C. Sun, H. Gao and Z. Liu, "Design of spatial adaptive cable-driven parallel robots with an unlimited rotation axis using the cable wrapping phenomenon," *Mech. Mach. Theory* **166**, 104475 (2021).
[15] R. Kelaiaia and A. Zaatri, "Multiobjective optimization of parallel kinematic mechanisms by the genetic algorithms," *Robotica* **30**(5), 783–797 (2012).
[16] Y. Qi, T. Sun and Y. Song, "Multi-objective optimization of parallel tracking mechanism considering parameter uncertainty," *J. Mech. Robot.* **10**(4), 041006 (2018).
[17] Y. Zhuo, T. Zhang, F. Du and R. Liu, "A parallel particle swarm optimization algorithm based on GPU/CUDA," *Appl. Soft Comput.* **144**, 110499 (2023).
[18] B. Zhou, S. Li, B. Zi, B. Chen and W. Zhu, "Multi-objective optimal design of a cable-driven parallel robot based on an adaptive adjustment inertia weight particle swarm optimization algorithm," *J. Mech. Design* **145**(8), 083301 (2023).
[19] P. Mandal and S. C. Mondal, "Multi-objective optimization of Cu-MWCNT composite electrode in electro discharge machining using MOPSO-TOPSIS," *Measurement* **169**, 108347 (2021).
[20] Q. Song, Z. Wang and T. Wu, "Risk analysis and assessment of water resource carrying capacity based on weighted gray model with improved entropy weighting method in the central plains region of China," *Ecol. Indic.* **160**, 111907 (2024).
[21] P. Chen, "Effects of the entropy weight on TOPSIS," *Expert Syst. Appl.* **168**, 114186 (2021).
[22] K. M. Lee and D. K. Shah, "Kinematic analysis of a three-degrees-of-freedom in-parallel actuated manipulator," *IEEE J. Robot. Autom.* **4**(3), 354–360 (1988).
[23] C. Yang, Q. Li and Q. Chen, "Multi-objective optimization of parallel manipulators using a game algorithm," *Appl. Math. Modell.* **1**(74), 217–243 (2019).
[24] B. Bounab, "Multi-objective optimal design based kineto-elastostatic performance for the delta parallel mechanism," *Robotica* **34**(2), 258–273 (2016).
[25] J. Wang, C. Wu and X. J. Liu, "Performance evaluation of parallel manipulators: Motion/force transmissibility and its index," *Mech. Mach. Theory* **45**(10), 1462–1476 (2010).
[26] J. Angeles, ed. Fundamentals of Robotic Mechanical Systems: Theory, Methods, and Algorithms (Springer New York, New York, NY, 2003).
[27] A. Klimchik, Enhanced Stiffness Modeling of Serial and Parallel Manipulators for Robotic-Based Processing of High Performance Materials PhD diss (Ecole Centrale De Nantes (ECN); Ecole Des Mines De Nantes, 2011).
[28] K. Deb, A. Pratap, S. Agarwal and T. A. Meyarivan, "A fast and elitist multiobjective genetic algorithm: NSGA-II," *IEEE Trans. Evol. Comput.* **6**(2), 182–197 (2002).

Cite this article: S. Yao, F. Liu, H. Mo, H. Gong, Y. Chen and T. Yang (2026). "Multi-objective optimization of a dish parabolic concentrator with a parallel sun-tracking mechanism", Robotica **44**, 723–738. https://doi.org/10.1017/S0263574726103294

https://doi.org/10.1017/S0263574726103294 Published online by Cambridge University Press